MTLA 49 (2026) 102860

Contents lists available at ScienceDirect

Materialia

journal homepage: www.elsevier.com/locate/mtla

Full Length Article

Introducing high-entropy to metal-organic-halide perovskite derivatives

Anurag Khandelwal [a], Evgeniy Boltynjuk [a], Holger Röhm [b,c], Simon Schweidler [a], Alexander Colsmann [b,c,*], Jasmin Aghassi-Hagmann [a,**], Ben Breitung [a,**]

[a] Institute of Nanotechnology, Karlsruhe Institute of Technology, Kaiserstraße 12, 76133, Karlsruhe, Germany
[b] Material Research Center for Energy Systems, Karlsruhe Institute of Technology, Kaiserstraße 12, 76133, Karlsruhe, Germany
[c] Light Technology Institute, Karlsruhe Institute of Technology, Kaiserstraße 12, 76133, Karlsruhe, Germany

ARTICLE INFO

Keywords:
High-entropy materials
High-entropy Iodides
Optical properties
Mechanical properties

ABSTRACT

The concept of high-entropy materials (HEMs) features the integration of multiple elements into a single phase, unlocking vast compositional freedom and yielding new functionalities. While oxides, sulphides, and nitrides have been widely explored, high-entropy iodides (HEIs) remain vastly unknown despite the rich optoelectronic properties of iodide perovskites. Here, we introduce low-dimensional perovskite derivative high-entropy iodides based on the $MA_3Bi_2I_9$ structure, synthesised via mechanochemical routes with systematic multi-cation substitution (Sn, Ag, Bi, Cu, Sb, Ca, Na, and In). X-ray diffraction confirms the formation of single-phase HEI, with phase purity depending strongly on elemental choice. The optical band gap is robust against compositional complexity while allowing the fine-tuning within 2.0–2.1 eV, indicating that electronic properties can be delicately adjusted without structural destabilisation. In contrast, mechanical properties vary almost by an order of magnitude, with Young's moduli spanning from 1.5 to 9.6 GPa, establishing a direct link between cation chemistry and lattice rigidity. These results demonstrate that high-entropy iodides are synthetically accessible, structurally stable, and provide a new platform for the fine-tuning of optical properties. At the same time, mechanical responses are widely adjustable by design, altogether opening previously unexplored compositional space for halide perovskite derivatives in optoelectronic and energy applications.

1. Introduction

High-entropy materials (HEMs) represent a rapidly emerging class of solids, distinguished by the incorporation of multiple elements at the same lattice position and the resulting stabilisation of single-phase crystal structures through high configurational entropy. Unlike conventional materials, where one or two dominant elements typically dictate properties, HEMs derive their characteristics from the complex interactions among multiple atomic species. This enables a vast compositional space, allowing the design of materials with tailored properties for specific applications. The concept was initially investigated in metallic systems, such as high-entropy alloys [1,2] and later extended to high-entropy oxides (ceramics) [3–6] encompassing a wide range of cations and anions. Recent advances have demonstrated the feasibility of fluorides [7] sulphides [8] nitrides [9] carbides [10] and mixed-anion compounds, such as oxyfluorides [11].

Halides, in particular, represent a promising yet underexplored class of high-entropy materials. Their structural flexibility and tunable electronic properties make them attractive for energy storage [12–14] catalysis [15] and optoelectronics applications [16]. For instance, high-entropy fluorides are widely employed in conversion-based batteries due to their high redox stability, while chlorides and bromides have been investigated as potential solid electrolytes [17–19]. Despite these advances, high-entropy iodides (HEIs) remain largely unexplored, even though iodide-based materials are well known for their catalytic activity [15] and semiconducting properties [20,21]. Their strong optical absorption in the UV/Vis spectral range, high charge carrier mobility, and low recombination losses make them particularly relevant for optoelectronic applications, including solar light harvesting [22].

The archetypal methylammonium lead iodide ($MAPbI_3$) represents a class of excellent light-harvesting semiconductors with efficient charge carrier transport [22]. Concerns about stability and toxicity, particularly regarding lead, have driven the search for alternative compositions [23]. A promising surrogate is the class of triple perovskites, such as

* Corresponding author at: Material Research Center for Energy Systems, Karlsruhe Institute of Technology, Kaiserstraße 12, 76133, Karlsruhe, Germany.
** Corresponding authors.
E-mail addresses: alexander.colsmann@kit.edu (A. Colsmann), jasmin.aghassi@kit.edu (J. Aghassi-Hagmann), ben.breitung@kit.edu (B. Breitung).

https://doi.org/10.1016/j.mtla.2026.102860
Received 18 May 2026; Accepted 30 July 2026
Available online 31 July 2026
2589-1529/© 2026 The Author(s). Published by Elsevier Inc. on behalf of Acta Materialia Inc. This is an open access article under the CC BY license (http://creativecommons.org/licenses/by/4.0/).

methylammonium bismuth iodide ($(CH_3NH_3)_3Bi_2I_9$), where lead is replaced with bismuth while maintaining suitable electronic and optical properties for photovoltaic applications [24]. Incorporating organic cations, such as methylammonium ($CH_3NH_3^+$), is crucial for stabilising the crystal lattice, modifying the band structure, and influencing charge-carrier transport [25,26].

Expanding the high-entropy material concept to iodides introduces additional complexity, particularly when integrating organic components. These arise from the temperature constraints imposed by the low decomposition temperatures of organic molecules and their increased sensitivity to environmental conditions and to the solvents used in solution-based synthesis techniques. Unlike purely inorganic high-entropy compounds, hybrid organic-inorganic systems require consideration of hydrogen bonding and steric effects, which can favour specific orientational arrangements, as well as electronic interactions between organic and inorganic sublattices. This additional degree of compositional freedom broadens the range of tunable properties and presents new challenges in understanding the structure-property relationships in these materials [27,28]. Moreover, the higher energy requirements for forming a high-entropy phase may result in the decomposition of organic precursors during synthesis.

This study investigates the synthesis, structure, and properties of low-dimensional perovskite derivative high-entropy iodides ($A_3B_2X_9$, X=I), where the B-site is populated by a mixture of up to six cations. By systematically varying the elemental composition, we elucidate the effects of multi-element interactions on crystal structure, electronic, optoelectronic, and mechanical properties, and discuss their potential for future applications.

2. Results and discussion

2.1. Design and synthesis of high-entropy iodides

High-entropy materials rely on the deliberate combination of multiple elements at a single crystallographic site, requiring careful consideration of ionic radii, oxidation states, and charge compensation to enable single-phase formation. In the case of hybrid halide perovskite derivatives, this challenge is further amplified by the presence of organic cations and the limited thermal stability of iodide frameworks. Here, we outline the rationale behind the selected multication compositions, focusing on entropy-driven mixing at the B-site of the $MA_3Bi_2I_9$ structure and the constraints that govern phase formation in these chemically complex systems.

The elements selected for the high-entropy compositions included Sn, Ag, Bi, Cu, Sb, Ca, Na, and In. Their selection was guided by crystal-chemical considerations, including ionic radius, oxidation state, charge balance, preferred coordination environment, and previous reports demonstrating structural compatibility with halide perovskite-related compounds. Based on the Shannon ionic radii for six-fold coordination, corresponding to the octahedrally coordinated B-site, Bi^{3+} (1.03 Å) was partially substituted by cations spanning a broad range of ionic radii, including Sb^{3+} (0.76 Å), Cu^{+} (0.77 Å), In^{3+} (0.80 Å), Ca^{2+} (1.00 Å), Na^{+} (1.02 Å), Sn^{2+} (1.02 Å), and Ag^{+} (1.15 Å). Thus, the selected cations do not all fulfil a simple similar-size criterion. Instead, the deliberate variation in ionic size and oxidation state was used to explore the crystal-chemical limits of multication substitution in the $MA_3Bi_2I_9$-type framework. Trivalent cations such as Sb^{3+} and In^{3+} were included because they provide chemically plausible B-site substitutions, whereas mono- and divalent cations were incorporated to achieve charge-balanced multication compositions. Together, the selected cations provide a chemically diverse compositional space for systematically investigating how multication substitution affects phase formation and composition–structure–property relationships in hybrid iodides.

The substantial ionic-size mismatch, particularly for Sb^{3+}, Cu^{+}, and In^{3+} relative to Bi^{3+}, is expected to introduce local lattice distortions and to increase the enthalpic penalty for forming a single multication $MA_3Bi_2I_9$-type phase. In metallic solid solutions, Hume-Rothery-type size criteria provide useful empirical guidelines, and size mismatches above approximately 15% are generally considered unfavourable for complete solid-solution formation. In hybrid halide perovskite derivatives, this criterion cannot be transferred directly because phase formation is additionally governed by metal–iodide bonding, charge compensation, coordination chemistry, framework dimensionality, and interactions with the organic methylammonium cation. Nevertheless, the observed phase-purity trend from HEI-1 to HEI-8 is consistent with the increasing crystal-chemical mismatch limiting the formation of a single $MA_3Bi_2I_9$-type phase.

Many of these elements have been extensively studied in perovskite systems, showing structural stability in various pairs. For instance, element pairs such as Ag-Bi, Cu-In, and Ag-Sb have been successfully incorporated into perovskite structures, demonstrating stability, narrow band gaps (<1.5 eV), and electron mobilities similar to those of $MAPbI_3$ [29]. Drawing upon these established findings, the properties of these element combinations can be extrapolated to predict their properties within the high-entropy framework, as fundamental structure-property relationships are generally retained across high-entropy systems. This highlights the potential for improving upon the stability and properties in this new material system.

The high-entropy iodides investigated in this work were synthesised using a mechanochemical ball-milling approach, which promotes intimate mixing of the precursor species and facilitates multication incorporation into the $MA_3Bi_2I_9$ framework. Mechanochemical synthesis has previously proven to be an effective route for the preparation of a wide range of high-entropy materials [30]. The influence of the milling parameters on phase formation is discussed below.

After ball milling, powders of the HEIs listed in Table 1 were obtained. Methylammonium occupies the A-site and iodide the X-site of the perovskite. The B-site contains combinations of different metal cations. While the compositional design defines the accessible chemical space, assessing the impact of multication substitution requires a clear structural reference. Therefore, the crystallographic motif of the parent $MA_3Bi_2I_9$ framework is first considered to establish the baseline against which entropy-induced structural effects can be evaluated.

2.2. Structural motif and structural stability of the MA3Bi2I9 framework

Before addressing entropy-induced effects, it is essential to establish the underlying structural motif of the investigated compounds. $MA_3Bi_2I_9$ represents a low-dimensional perovskite derivative composed of discrete $[Bi_2I_9]^{3-}$ units separated by organic cations, offering a structurally flexible yet well-defined framework. In this section, the crystallographic characteristics of the parent structure are briefly summarised, providing the structural reference necessary to assess how extensive multication substitution can be accommodated without disrupting the fundamental $MA_3Bi_2I_9$ framework.

The $MA_3Bi_2I_9$ crystal structure consists of inorganic bismuth-iodide units and organic $(CH_3NH_3)^+$ cations. Structurally, $MA_3Bi_2I_9$ features Bi_2I_9 dioctahedral units, where each Bi^{3+} ion is coordinated by six iodide ions, forming face-sharing $[BiI_6]$ octahedra (Fig. 1). $MA_3Bi_2I_9$ can form two polymorphs, where these Bi_2I_9 units constitute either a layered (2D)

Table 1
Synthesised triple-perovskite high-entropy iodides.

Acronym	Composition
HEI-1	$(CH_3NH_3)_3(Sn_{0.2}Ag_{0.2}Bi_{0.2}Cu_{0.2}Sb_{0.2})_2I_9$
HEI-2	$(CH_3NH_3)_3(Sn_{0.16}Ag_{0.16}Bi_{0.16}Cu_{0.16}Sb_{0.16}Ca_{0.16})_2I_9$
HEI-3	$(CH_3NH_3)_3(Sn_{0.2}Ag_{0.2}Bi_{0.2}Na_{0.2}Sb_{0.2})_2I_9$
HEI-4	$(CH_3NH_3)_3(Sn_{0.16}Ag_{0.16}Bi_{0.16}Na_{0.16}Sb_{0.16}Ca_{0.16})_2I_9$
HEI-5	$(CH_3NH_3)_3(Sn_{0.2}Ag_{0.2}Bi_{0.2}Cu_{0.2}In_{0.2})_2I_9$
HEI-6	$(CH_3NH_3)_3(Sn_{0.16}Ag_{0.16}Bi_{0.16}Cu_{0.16}In_{0.16}Ca_{0.16})_2I_9$
HEI-7	$(CH_3NH_3)_3(Sn_{0.2}Ag_{0.2}Bi_{0.2}Na_{0.2}In_{0.2})_2I_9$
HEI-8	$(CH_3NH_3)_3(Sn_{0.16}Ag_{0.16}Bi_{0.16}Na_{0.16}In_{0.16}Ca_{0.16})_2I_9$

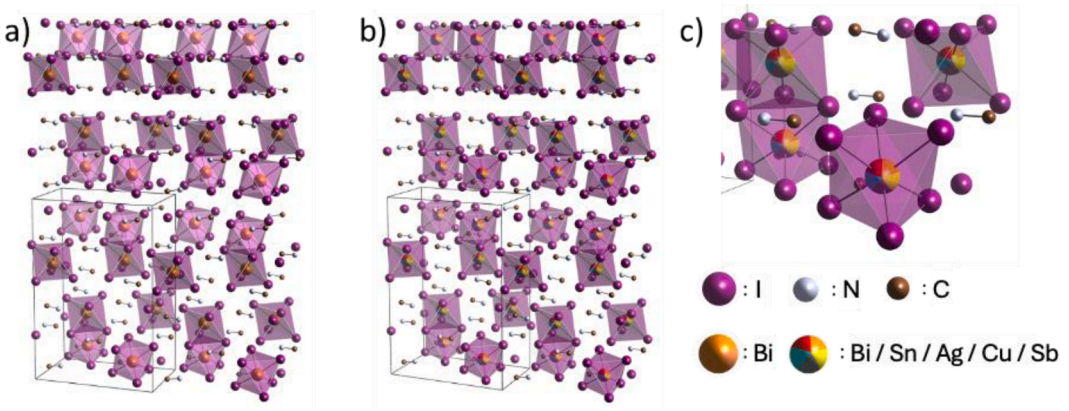

Fig. 1. a) Crystal structure of $MA_3Bi_2I_9$. Bi^{3+} ions are coordinated to I- ions, forming a molecular complex that is distinctly isolated rather than forming extended networks or layers. The $[Bi_2I_9]^{3-}$ units are characterised by I- ions bridging two Bi3+ ions. The discrete $[Bi_2I_9]^{3-}$ units, spatially separated by the organic cations, form a 0D structure with minimal interaction between the $[Bi_2I_9]^{3-}$ units. b) High-entropy triple perovskite. Other elements partially replace the Bi3+ positions, while the crystal structure persists. c) Detailed representation of the high-entropy $[Bi_2I_9]^{3-}$ units. Having established the structural characteristics of the $MA_3Bi_2I_9$ framework, the question arises under which conditions this motif can be preserved in a chemically complex, multicationic environment. The following section therefore examines the phase evolution during mechanochemical synthesis and the role of structural stabilisation.

or a zero-dimensional (0D) structure. The $(CH_3NH_3)^+$ cations are incorporated between the bismuth-iodide units, playing a crucial role in stabilising the structure via electrostatic interactions and hydrogen bonding with the iodide ions. In 3D perovskite structures (e.g., $MAPbI_3$), the organic cation primarily adjusts the geometry of the 3D corner-sharing BX_6 network, leading to octahedral tilting and helping determine the stable polymorph based on symmetry. In $MA_3Bi_2I_9$, $(CH_3NH_3)^+$ plays a role in organising the packing, affects the dimensionality (0D or 2D), and can significantly impact both optical and electronic properties.

2.3. Phase evolution and structural stability

The formation of a single-phase high-entropy compound is governed not only by composition but also by the energetic pathways available during synthesis. Mechanochemical processing provides a unique route to access such phases by supplying high local energies while avoiding thermal decomposition of organic components. In this section, X-ray diffraction is used to track the phase evolution during milling, revealing the critical role of milling energy and duration in driving the transformation from mixed precursors to a high-entropy $MA_3Bi_2I_9$-type structure.

The structures of the synthesised HEIs were analysed using X-ray diffraction (XRD) to verify the successful formation of the $MA_3Bi_2I_9$ phase (Fig. 2). The measured XRD diffractograms of the HEIs match most closely with the $MA_3Bi_2I_9$ structure (ICSD database code 242181), which is a 0D structure with the space group *C*2/*c*. While HEI-1, HEI-2, and HEI-3 predominantly exhibit single-phase structures similar to $MA_3Bi_2I_9$, the remaining compositions are either multiphase or not clearly defined crystallographically in publicly available databases. Fig. 2a provides an overview of the diffractograms of all compositions, while Fig. 2b presents a more detailed view of the predominantly single-phase HEIs. While HEI-1 exhibits the highest phase purity and crystallinity, HEI-2 and HEI-3 show additional reflections (indicated by asterisks). Henceforth, the study focusses on the structurally best-defined compositions, HEI-1, HEI-2 and HEI-3, with special focus on HEI-1 which exhibited the highest purity of all samples under investigation.

Rietveld refinement was carried out with the *C*2/*c* structure, as shown in Fig. 3, confirming the formation of a single-phase structure. The structure exhibits a distorted lattice with a cell volume 1.25 % more than the ideal $(CH_3NH_3)_3Bi_2I_9$ structure. The R_{wp} is 4.86, and the goodness of fit is 4.47 for the refinement. The refined lattice parameters obtained from the Rietveld refinement are $a = 8.562(3)$ Å, $b = 14.802(5)$

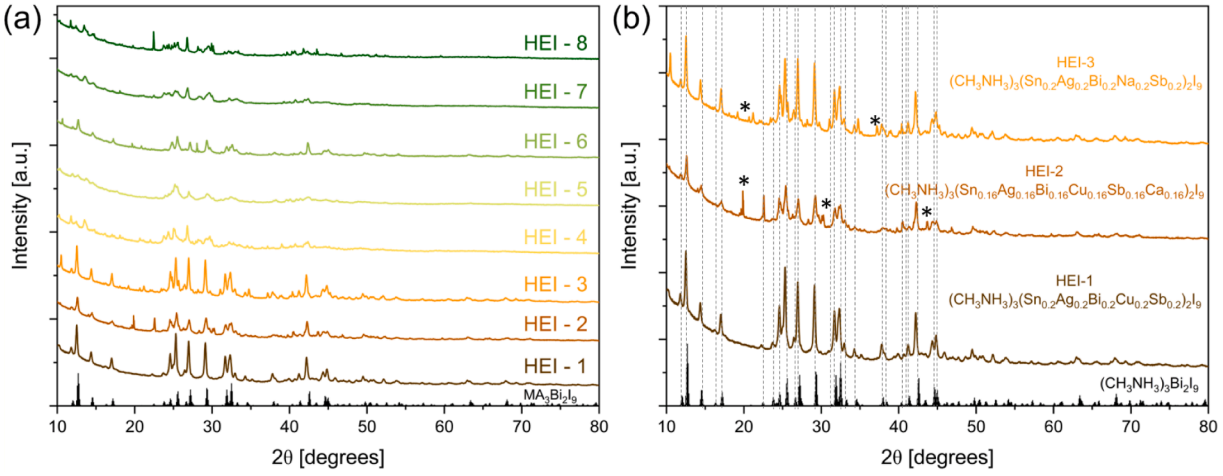

Fig. 2. a) XRD patterns of all synthesised HEIs and (CH3NH3)3Bi2I9 for reference. While HEI-1, HEI-2, and HEI-3 exhibit a predominant C2/c structure, the other compositions display significantly reduced crystallinity, challenging the determination of their structure. b) More detailed XRD patterns of HEI-1, HEI-2, and HEI-3. HEI-1 shows the highest purity and crystallinity. All compositions show the C2/c structure; some additional reflections are found and are marked with asterisks.

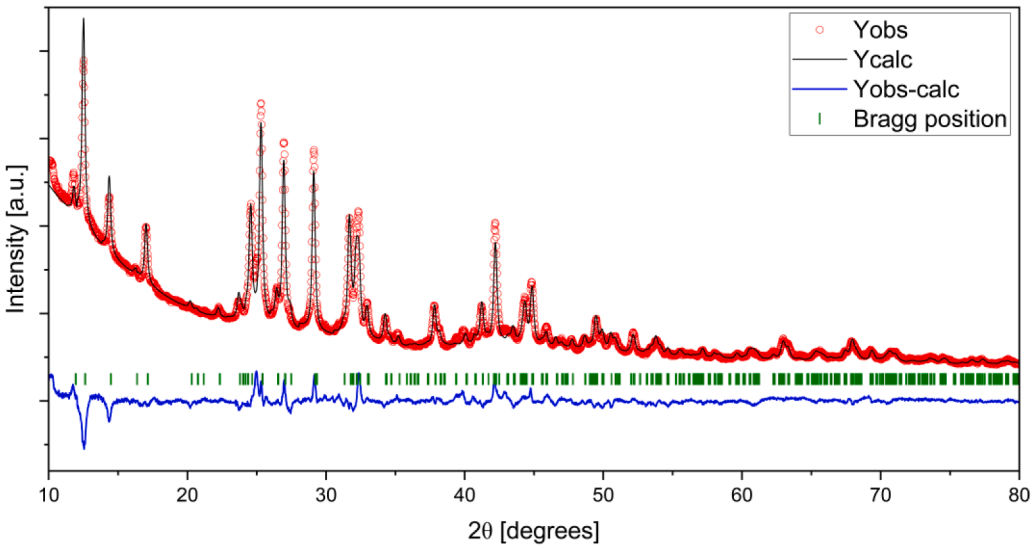

Fig. 3. Rietveld refinement of the powder X-ray diffraction pattern of HEI-1.

Å, and $c = 21.6522(6)$ Å, corresponding to a unit-cell volume of $V = 2744.26(1.44)$ Å^3. The increased cell volume compared with the reference $MA_3Bi_2I_9$ structure indicates a measurable expansion of the $MA_3Bi_2I_9$-type framework upon multication substitution.

Although all eight high-entropy iodide compositions were successfully synthesised, the extent of secondary phase formation increased progressively from HEI-4 onwards. Since the objective of this work is to establish intrinsic structure–property relationships, the detailed optical and mechanical investigations were focused on HEI-1 to HEI-3, which exhibited the highest structural quality and therefore allow the most reliable interpretation of composition-dependent effects.

This trend can be rationalised using crystal-chemical descriptors that are commonly applied to high-entropy perovskites and related high-entropy ceramics [31]. In such systems, single-phase formation is not governed by configurational complexity alone, but by the balance between ionic-size mismatch, charge balance, oxidation-state compatibility, preferred coordination environment, and the ability of the crystal framework to accommodate local lattice distortions. Large size mismatch or incompatible coordination preferences can increase the enthalpic penalty for multication incorporation and thereby promote secondary phase formation. Although these concepts were mainly developed for inorganic oxide perovskites and cannot be transferred directly to the low-dimensional hybrid $MA_3Bi_2I_9$-type framework, they provide a useful qualitative guideline for the present system. Accordingly, the increasing secondary phase formation from HEI-4 onwards is consistent with increasing crystal-chemical mismatch and charge-compensation complexity, which limit the formation of a single multication $MA_3Bi_2I_9$-type phase.

Aliquots of HEI-1 from the milling jar were taken and analysed throughout the milling process to monitor the formation of the structure during the mechanochemical synthesis. To avoid significant changes in the ball-to-powder ratio during the milling process, only micrograms of the powder were extracted. The milling speed was also steadily increased to facilitate better observation of the development with an increase in milling power, and consequently, the energy transfer associated with the thermal effects of collisions.

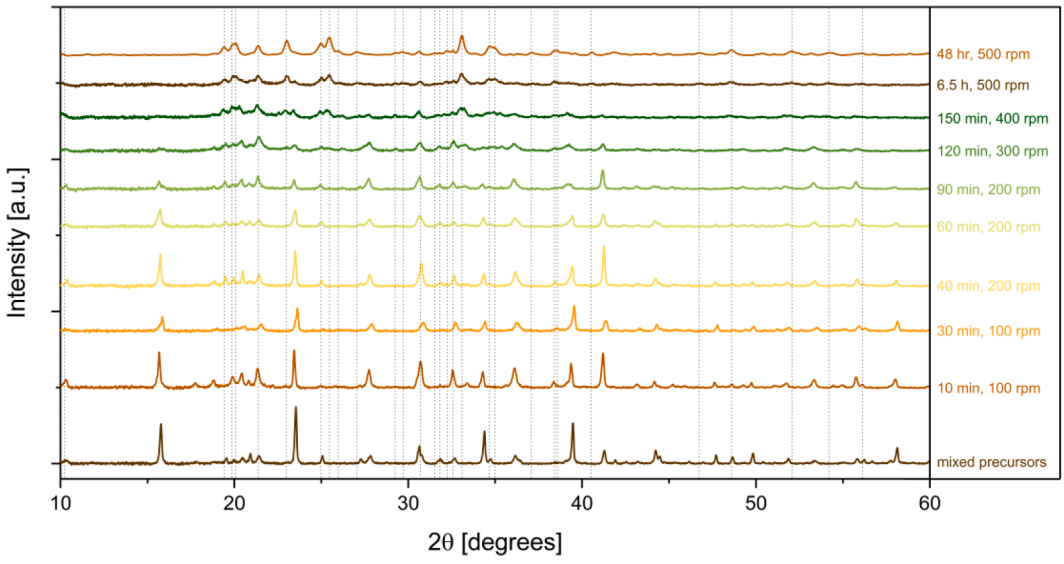

Fig. 4. From bottom to top: Structural development of HEI-1 for increasing milling power; the dotted lines mark the major peaks associated with the structure of MA3Bi2I9. The signatures of the mixed precursors are visible in the XRD pattern up to a rotation speed of 300 rpm. At higher rotation speeds, the C2/c structure forms.

In Fig. 4, the XRD data of HEI-1 collected throughout the milling process indicate that both prolonged milling durations and high rotational speeds are necessary to synthesise the high-entropy iodides and to achieve the desired phase. At lower milling speeds up to 300 rpm, the reflections of the precursor mixture show decreased intensities and slightly broadened peaks, which can be attributed to the reduction in crystallite sizes of the precursors caused by the milling process. However, no transformation to the target phase occurs at lower milling speeds. At 300 - 400 rpm, the first transformations become visible in the XRD patterns, and their signatures remain relatively constant even at 500 rpm. A long milling time of 48 h at 500 rpm was required to obtain broad but distinguishable reflections, indicating the formation of the $MA_3Bi_2I_9$-type structure.

The broad diffraction peaks observed after extended milling are characteristic of mechanochemically synthesised powders and should not be interpreted as direct evidence of amorphization. High-energy ball milling commonly leads to the formation of nanocrystalline materials with small crystallite sizes, high defect densities, and microstrain, all of which contribute to diffraction peak broadening. In the present case, the gradual disappearance of the precursor reflections and the simultaneous emergence of the characteristic $MA_3Bi_2I_9$-type reflections indicate successful phase formation during milling. At the same time, no pronounced amorphous halo is observed in the XRD patterns, suggesting that significant amorphization does not occur under the applied milling conditions. The remaining peak broadening is therefore attributed primarily to the nanocrystalline and defect-rich nature of the mechanochemically synthesised HEI powders.

Mechanochemical synthesis produces stable $MA_3Bi_2I_9$-type high-entropy iodides; however, high milling energy and extended duration are critical for achieving phase purity. This highlights the need for larger energetic inputs to achieve crystallographic stability in HEMs.

Attenuated total reflection infrared spectroscopy (ATR-IR) measurements determined whether the $(CH_3NH_3)^+$ ion decomposed during mechanochemical synthesis or was incorporated into the structure. The characteristic vibrations of the $(CH_3NH_3)^+$ ion were observed (Fig. 5), indicating that the molecule remained after the synthesis [32]. Moreover, the distinct absence of any metal iodide phases in the XRD patterns implies that the $A_3B_2I_9$ stoichiometry is maintained in the product. Since the A-site is predominantly occupied by $(CH_3NH_3)^+$ amongst the chosen cations, this, combined with the ATR-IR spectroscopy results, indicates that $(CH_3NH_3)^+$ did not undergo significant decomposition during the high-energy synthesis process.

While XRD and ATR-IR confirm the formation of an $MA_3Bi_2I_9$-type phase, they do not directly verify homogeneous multication incorporation or the integrity of the hybrid framework. To address this, complementary spectroscopic and compositional analyses are employed to validate the high-entropy nature of the synthesised compounds.

2.4. Verification of multication incorporation and structural integrity

Demonstrating true high-entropy behaviour requires verification that all intended elements are incorporated into a single phase while preserving the integrity of the hybrid framework. Given the beam sensitivity and mechanical softness of iodide perovskites, complementary characterisation techniques are required to validate multication incorporation and structural stability. Here, a combination of infrared spectroscopy, elemental analysis, and morphology-sensitive probes is employed to confirm the preservation of the methylammonium cation and the homogeneous incorporation of all B-site elements.

Fig. 6a shows a scanning electron microscopy (SEM) image of gold-coated HEI-1 powder with a very short focusing time. The surface exhibits significant roughness, with small particles of 200 nm diameter protruding from the surface. Since metal iodides are notorious for being damaged during investigation by SEM or transmission electron microscopy (TEM) [33], an area damaged by the electron beam of the SEM is visible in the right part of the image. Therefore, the powders were pressed into pellets, and then the HEI surface was also investigated by atomic force microscopy (AFM). Yet, the soft nature of the HEIs challenged AFM imaging. Fig. 6b and 6c show the amplitude and amplitude error of the AFM measurements of the HEI-1 pellet. Both measurements indicate a rough surface with small particles growing. Fig. 6d shows an SEM image of the surface of the pressed pellet, where it forms a highly uniform surface. The absence of small particles, compared to the powder morphology, indicated an affinity for homogeneous plastic deformation under pressure application.

The elemental concentrations in the samples were measured using X-ray fluorescence (XRF), and the results are presented in Fig. 7. The measured B-site compositions are close to the expected equiatomic

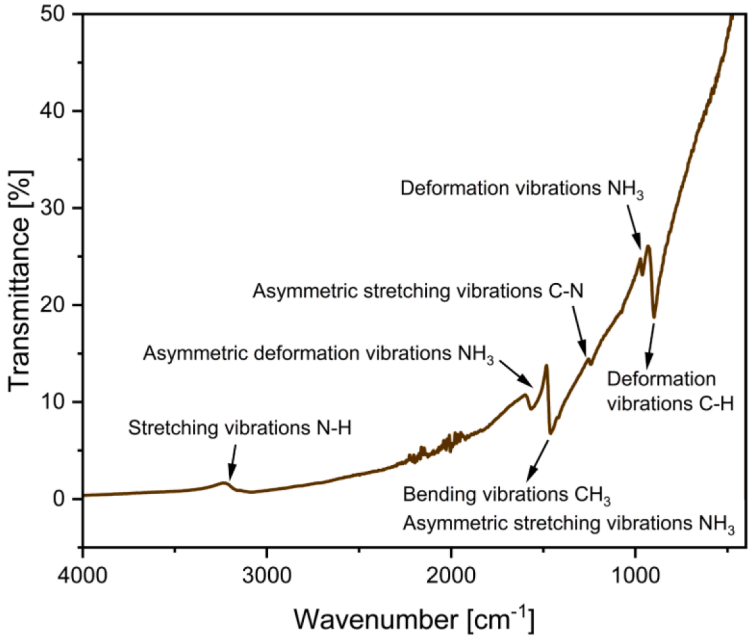

Fig. 5. ATR-IR spectrum of HEI-1. The typical vibrational/stretching nodes of (CH3NH3)+ can be observed; the asymmetric vibrational/stretching node for C—N also indicates that (CH3NH3)+ persists during the synthesis by ball milling.

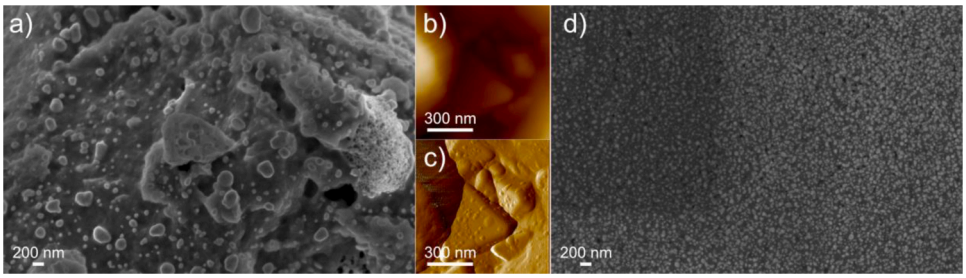

Fig. 6. a) SEM image of gold-coated HEI-1 powder captured at a low accelerating voltage of 5 kV, b) AFM amplitude, c) AFM amplitude error, and d) SEM image of gold-coated HEI-1 pellet.

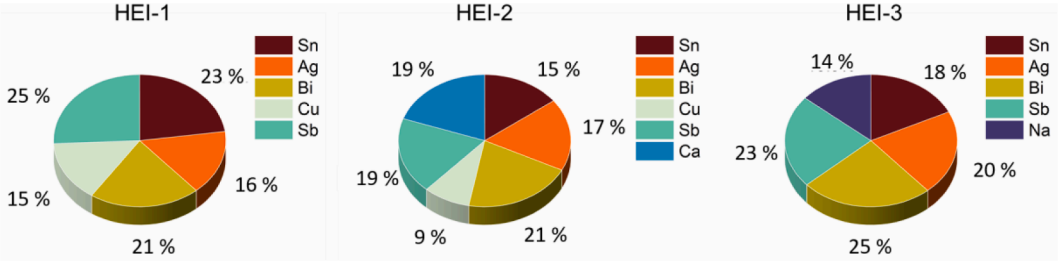

Fig. 7. Concentration of B-site elements in the compounds HEI-1, HEI-2, and HEI-3 from XRF.

concentrations. The observed deviations from the nominal values are within the range expected from sample preparation and processing, including weighing, powder handling, and possible material loss during ball milling. The XRF results therefore confirm the presence of all intended metal elements in the final powders and show that their relative concentrations remain close to the nominal compositions. In combination with the XRD results, which confirm the formation of the $MA_3Bi_2I_9$-type phase and reveal possible secondary phases, these data support the successful preparation of multication high-entropy iodides.

Despite the intrinsic mechanical softness and instability of the HEIs under electron irradiation, altogether, the different measurements confirm that all precursor elements are incorporated and that the $(CH_3NH_3)^+$ cation remains intact, verifying successful synthesis of multi-cationic HEIs. With the successful incorporation of all constituent elements and preservation of the hybrid structure established, the consequences of multication disorder on functional properties can now be addressed. Given the known mechanical softness of iodide perovskites, mechanical response represents a particularly sensitive probe of complexity-induced lattice effects.

2.5. Complexity-sensitive mechanical response and design rules

While the crystal structure of the investigated high-entropy iodides remains largely conserved, their mechanical response is expected to be highly sensitive to local bonding environments and charge distribution. Multication substitution introduces significant variations in ionic size, valence, and bonding character, which can profoundly influence lattice rigidity and deformation behaviour. In this section, nanoindentation measurements reveal pronounced differences in Young's modulus and hardness, enabling the extraction of clear composition–mechanics design rules for entropy-engineered iodide perovskites.

Under the application of pressure during ATR-IR sample preparation and pellet formation, HEI-1 exhibited flux-like behaviour similar to KBr. This qualitative observation already indicates that mechanical properties in high-entropy iodides are highly sensitive to cation chemistry, in strong contrast to their comparatively robust optical response discussed below. Individual particles cold-flow under pressure, plastically deforming and assuming the shape of the pellet die without fracturing. The pellets were prepared by cold pressing at room temperature without additional thermal treatment. To verify that pressing does not induce a major phase transformation, XRD patterns of the pristine powder and pressed material were compared on a common d-spacing scale, accounting for the different X-ray wavelengths used for the measurements. The characteristic reflections of the $MA_3Bi_2I_9$-type phase are retained after pressing, and the peak positions of the pressed material can be indexed using the same monoclinic *C*2/*c* structure as the pristine powder. The lattice parameters obtained from this peak-position analysis are approximately $a = 8.545$ Å, $b = 14.815$ Å, and $c = 21.650$ Å, corresponding to a unit-cell volume change of only approximately 0.13% compared with the pristine powder. No additional systematic set of reflections indicative of a major structural transformation is observed. The average *C*2/*c* structure is therefore preserved under the applied pressing conditions, while the changes in relative reflection intensities and peak shapes are mainly attributed to pressure-induced preferred orientation, crystallite rearrangement, and microstructural changes during plastic deformation. The corresponding comparison is shown in **Fig. S1**. To investigate whether the mechanical properties of HEI pellets depend on their elemental composition, the three highly single-phase compounds HEI-1, HEI-2, and HEI-3 were subjected to nanoindentation measurements (Table 2). Typical Young's moduli of perovskites with organic cations such as $(CH_3NH_3)^+$ range from 1 to 10 GPa [34,35]. HEI-1, HEI-2, and HEI-3 fall within this range; however, it is evident that the elemental combination can induce significant changes in the mechanical properties.

Table 2
Hardness and Young's moduli of the compounds HEI-1, HEI-2, and HEI-3.

Abbreviation	Cationic composition at B-site	Hardness (GPa)	Young's modulus (GPa)	Mechanical properties
HEI-1	Sn, Ag, Bi, Cu, Sb	0.17	9.58	Comparatively stiff, yet plastically compliant
HEI-2	Sn, Ag, Bi, Cu, Sb, *Ca*	0.04	1.49	Soft lattice, pronounced creep-like behaviour
HEI-3	Sn, Ag, Bi, Sb, *Na*	0.05	1.81	Very soft, pronounced creep-like behaviour

The investigated HEIs exhibit notable differences in their mechanical properties, particularly in Young's modulus and hardness, which signifies different flow behaviours under applied mechanical load. HEI-1 exhibits a higher Young's modulus (9.6 GPa) and hardness (0.17 GPa), and thus displays a much stiffer and more resistant lattice structure than HEI-2 and HEI-3. This indicates a higher energy barrier for plastic deformation, consistent with a more brittle mechanical response. In contrast, HEI-2 and HEI-3, with lower Young's moduli (1.5 and 1.8 GPa, respectively) and hardnesses below 0.05 GPa, are much softer and thus potentially more prone to flow under applied stress. These reduced mechanical resistances facilitate local deformation, creep behaviour, and even macroscopic flow under moderate pressure, phenomena commonly observed in soft ionic solids. The pronounced differences in Young's modulus between the investigated HEI compositions should be interpreted with caution. Rietveld refinement of HEI-1 confirms that the sample retains the *C*2/*c* symmetry of the $MA_3Bi_2I_9$-type structure, with refined lattice parameters of $a = 8.562(3)$ Å, $b = 14.802(5)$ Å, and $c = 21.6522(6)$ Å, resulting in a unit-cell volume of $V = 2744.26(1.44)$ Å^3. Compared with the reference $MA_3Bi_2I_9$ structure, this corresponds to a measurable increase in unit-cell volume, indicating that multication substitution leads to detectable structural distortion or expansion of the framework. The differences in Young's modulus may therefore be related to changes in the local bonding environment caused by different charge states, ionic-size mismatch, and multication-induced distortion of the $MA_3Bi_2I_9$-type framework. However, the mechanical response cannot be assigned to lattice distortion alone. In particular, HEI-2 and HEI-3 contain minor secondary phases. These secondary phases may contribute to the measured mechanical response; however, they are unlikely to be the sole origin of the pronounced softening observed for HEI-2 and HEI-3, as both samples predominantly retain the $MA_3Bi_2I_9$-type structure and the additional reflections are weak compared with the main phase reflections. The systematic decrease in Young's modulus and hardness upon incorporation of Ca^{2+} in HEI-2 or Na^{+} in HEI-3 therefore suggests that B-site cation chemistry plays a dominant role in controlling the mechanical response. The addition of smaller cations to the system has been shown to increase the hardness and Young's modulus of perovskite systems through lattice compression effects [36, 37]. The key distinction among these compositions is the presence or absence of Ca^{2+} or Na^{+}. The strongest hardness is observed in the absence of both Ca^{2+} and Na^{+}, suggesting their incorporation leads to a softer structure. Although the exact mechanisms remain to be fully elucidated, the inclusion of Ca^{2+} and Na^{+} likely weakens the electrostatic interactions as alkali and alkali-earth metals tend to result in more ionic (less covalent) bonding, given their lack of d-orbital involvement. The crystal structure may exhibit enhanced covalency in the absence of these cations, contributing to greater rigidity. Furthermore, introducing Ca^{2+} or Na^{+} requires additional charge compensation to maintain an average cationic charge of 3+ throughout the crystal structure, disrupting the optimal charge balance and perturbing the local coordination environment. In $(CH_3NH_3)_3(Sn_{0.2}Ag_{0.2}Bi_{0.2}Cu_{0.2}Sb_{0.2})_2I_9$, elements such as Sb, Sn, and Bi can adopt higher oxidation states, which helps preserve a stable, stiffer structure. In contrast, the incorporation of Ca^{2+} in $(CH_3NH_3)_3(Sn_{0.16}Ag_{0.16}Bi_{0.16}Cu_{0.16}Sb_{0.16}Ca_{0.16})_2I_9$ and the substitution of Cu^{+}/Cu^{2+} by Na^{+} in $(CH_3NH_3)_3(Sn_{0.2}Ag_{0.2}Bi_{0.2}Na_{0.2}Sb_{0.2})_2I_9$ introduce lower-charge species that require compensation, leading to increased lattice distortions and a reduction in bonding strength. These factors collectively result in a more flexible, less rigid lattice, as evidenced by the significantly reduced Young's moduli of HEI-2 and HEI-3. Therefore, structurally, the enhanced flow propensity can be attributed to the incorporation of Ca^{2+} and Na^{+}, which, due to their low charge density and lack of d-orbital participation, weaken electrostatic bonding, disrupt charge balance, and reduce lattice cohesion. The increase in the ionic interactions in the lattice may increase migration barriers and thus reduce ionic mobility [38]. Overall, the mechanical profiles suggest that HEI-2 and HEI-3 may primarily serve as model ionic solids with pronounced flow behaviour, analogous to classical compounds like KBr, but with the added complexity and tunability of high-entropy chemistry.

The mechanical response of HEIs can thus be deliberately tailored by cation selection: transition-metal and semimetal cations (Sn, Sb, Bi) reinforce the lattice, whereas alkali and alkaline-earth cations (Na, Ca) drastically reduce stiffness. This establishes a clear design rule linking multication chemistry directly to mechanical compliance. The pronounced variations in mechanical properties demonstrate that complexity-driven multication substitution strongly perturbs lattice rigidity. In contrast, it remains to be clarified whether the optoelectronic properties are affected to a similar extent, or whether they remain governed by the underlying inorganic framework.

2.6. Complexity-insensitive optical properties

In contrast to their mechanical behaviour, the optoelectronic properties of halide perovskites are often governed by the inorganic framework and orbital interactions near the band edges. Whether extensive multication disorder significantly perturbs these electronic states remains an open question for high-entropy iodides. Here, optical absorption and photoelectron spectroscopy are used to assess the band gap and ionisation energy of the investigated compounds, revealing a remarkably robust optical response despite substantial compositional complexity. Since halide perovskites are widely used in optoelectronics, the effect of multication composition on the optoelectronic properties of HEI-1, HEI-2, and HEI-3 was investigated (Fig. 8). For this purpose, HEI-1, HEI-2 and HEI-3 were spin cast on glass substrates, and their absorption was measured using UV–Vis absorption spectrometry. The direct and indirect optical band gaps were determined using the Tauc plots. The direct band gap $E_{g,d}$ of a semiconductor can be derived by a linear fit to:

$$(\alpha h\nu)^2 = A\left(h\nu - E_{g.d}\right)$$

The indirect band gap $E_{g,i}$ of a semiconductor can be derived by a linear fit to:

$$(\alpha h\nu)^{0.5} = A\left(h\nu - E_{g.i}\right)$$

Here, α is the absorption coefficient near the band edge, $h\nu$ is the incident photon energy, E_g is the band gap, and A is the fitting constant. The band gaps can be determined by extrapolating the curve to the $(\alpha h\nu)^2 = 0$ (for direct band gaps) or $(\alpha h\nu)^{0.5} = 0$ (for indirect band gaps) axis.

Fig. 8a shows the absorbance spectra of the samples. The Tauc plots corresponding to the direct and indirect transitions are depicted in Fig. 8b and 8c, respectively. Indirect Tauc fits yield apparent band gaps between 1.31 and 1.56 eV; however, the consistently narrower spread and sharper linear onset of the direct transitions (between 2.04 and 2.11 eV) identify the direct band gap as the more physically relevant descriptor. The markedly sharper linear onset observed for the direct transitions strongly suggests that the investigated HEIs behave predominantly as direct-bandgap semiconductors. Previous studies [39–41] have reported direct band gaps for $MA_3Bi_2I_9$, and the dark-red visual appearance of the samples aligns with the observed band gap. Low-dimensional perovskite derivatives such as $MA_3Bi_2I_9$ are frequently discussed in terms of indirect optical transitions. While indirect Tauc fits can formally be applied, the markedly sharper absorption onset and the consistently linear behaviour observed for direct transitions indicate that the investigated HEIs behave predominantly as direct-bandgap semiconductors. Remarkably, the direct band gaps of the three HEIs remain nearly identical despite substantial differences in elemental composition and crystallinity. This indicates that, in contrast to mechanical properties, the optical band gap is largely insensitive to entropy-driven multication disorder. Considering the expected uncertainty of the optical band-gap determination, only minor differences are observed. This observation is notable given the substantial differences in

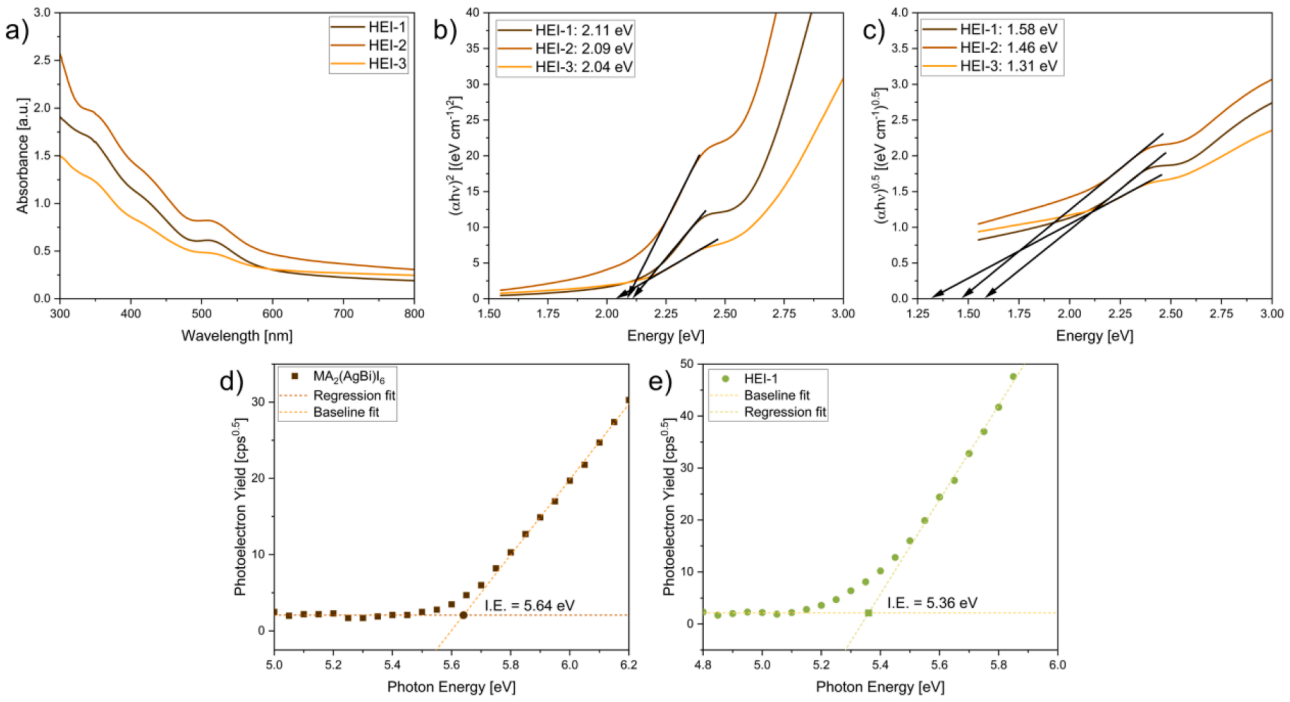

Fig. 8. a) UV–Vis absorbance of HEI-1, HEI-2, and HEI-3 thin films, b) and c) Tauc-plot fits indicate direct band gaps between 2.04 eV and 2.11 eV while indirect band gaps lie between 1.31 eV and 1.58 eV, d) and e) PESA measurements indicate ionisation energies of 5.64 eV and 5.36 eV of MA2(AgBi)I6 and HEI-1.

elemental composition and crystallinity, highlighting the robustness of the optical band gap against compositional complexity. Previous studies have reported direct band gaps of $MA_3Bi_2I_9$ derivatives between 2.1 and 2.4 eV [40–42] suggesting that while element substitution considerably affects crystal formation and mechanical properties, its effect on the band gap is small. A smaller band gap indicates a potential modification of the electronic structure resulting from the incorporation of multiple elements, which can influence charge-carrier dynamics and optical properties [42]. In the case of this high-entropy iodide structure, where different elements have replaced Bi, the band gap reduction between the different compositions may result from the local electronic interactions between the diverse cations. The mixed-element environment may subtly modify the electronic landscape near the band edges, as reflected by changes in the ionisation energy [38]. Such compositional complexity may influence charge-carrier energetics, warranting further investigation beyond the scope of this study.

Photoelectron spectroscopy in air (PESA) measurements were performed to determine the ionisation energy of the semiconductors (Fig. 8d and 8e) and referenced to $MA_2(AgBi)I_6$ [43]. The ionisation energies, determined from a fit of the linear regime in the PESA data, are 5.64 eV for $MA_2(AgBi)I_6$ and 5.36 eV for HEI-1. These differences indicate significant differences in electronic structure or density of states between the two semiconductors. The PESA measurements of $MA_2(AgBi)I_6$ and HEI-1 showed that achieving a comparable signal intensity required approximately 100 times higher UV excitation for $MA_2(AgBi)I_6$ (1000 vs. 10 nW). The lower photoelectron quantum efficiency of $MA_2(AgBi)I_6$ may be attributed to a lower absorption efficiency or a lower density of occupied electronic states, which reduces the contribution to photoemission. In contrast, the high-entropy composition of HEI-1 may exhibit an increased density of occupied states near the valence band maximum, facilitating more efficient photoelectron emission. This downward shift may also arise from a reduced contribution of the ns^2 states towards the valence band [44].

Across the investigated multicationic compositions HEI-1, HEI-2, and HEI-3, the direct optical band gaps lie within a narrow range of 2.0–2.1 eV. Considering the uncertainty associated with the experimental procedure and the selection of the linear fitting range in the Tauc analysis, these values should be regarded as very similar within experimental and fitting uncertainty. Therefore, the present data do not indicate a pronounced composition-dependent shift of the direct optical band gap among the three investigated compositions. This suggests that, for HEI-1 to HEI-3, the absorption edge remains primarily governed by the $MA_3Bi_2I_9$-type iodide framework. However, this conclusion is restricted to the structurally best-defined compositions investigated here. HEI-4 to HEI-8 were not included in the optical-property analysis because their increased secondary phase content and lower structural quality would make the extracted optical band gaps difficult to interpret and not directly comparable to those of HEI-1 to HEI-3. At the same time, changes in the ionisation energy indicate that the occupied electronic states can still be affected by the multication composition.

3. Conclusion

In this work, we demonstrate low-dimensional perovskite derivative high-entropy iodides, extending the high-entropy design strategy to iodide-based perovskites. The main findings of our work include:

- Structural stabilisation: Mechanochemical synthesis enables the formation of $MA_3Bi_2I_9$-type HEIs, but requires high milling energy and long duration, reflecting the delicate balance between compositional complexity and crystallographic stability.
- Elemental incorporation: Complementary spectroscopic and compositional analyses confirm full integration of all precursors and preservation of the MA cation, validating the synthesis of multicationic HEIs despite their intrinsic beam sensitivity.
- Mechanical versatility: Young's modulus and hardness vary several-fold depending on cation chemistry. Transition-metal and semimetal cations (Sn, Sb, Bi) reinforce the lattice, whereas main-group cations (Na^+, Ca^{2+}) drastically soften it, establishing a precise composition-mechanics design principle.
- Optical robustness with tunability: The direct band gap remains within a narrow window (2.0–2.1 eV) but can be fine-tuned by compositional choice, ensuring predictable optoelectronic performance. Subtle changes in the electronic structure could also tune the

ionisation energy and density of occupied states, as expected in such compositionally complex materials.

These findings demonstrate that high-entropy iodides uniquely combine complexity-insensitive optical properties with complexity-sensitive mechanical responses. This decoupling enables the independent tuning of optical performance and mechanical compliance through multication design, opening a previously unexplored design space for halide perovskite derivatives. Their unique structure–property relationships may enable tailored applications in photodetectors, solid-state ionics, or flexible optoelectronic coatings. Future work should focus on correlating induced lattice distortions with charge carrier dynamics and long-term stability, thereby paving the way for the development of functional HEI-based devices.

4. Experimental section

4.1. Synthesis of HEIs

The following chemicals were purchased from commercial sources and used without any further purification: $(CH_3NH_3)I$ (Ossila, >99.9%), AgI (Sigma-Aldrich, 99%), BiI_3 (Sigma-Aldrich, 99%), CuI (Sigma-Aldrich, 98%), SbI_3 (Sigma-Aldrich, 98%), CaI_2 (Sigma-Aldrich, 99%), InI_3 (Sigma-Aldrich, 99.998%), NaI (Alfa Aesar, >99.5%), and SnI_2 (Thermo Scientific, >99%).

Powder synthesis: The precursor iodides were added in equiatomic stoichiometries to a WC ball mill vial inside an argon atmosphere glovebox (Jacomex, <10 ppm O_2 and <1 ppm H_2O). 5 mm WC balls were used as the milling media, with a 20:1 ball-to-powder weight ratio. The ball mill vials were sealed inside the glove box to ensure an argon atmosphere within them, thereby preventing material degradation. The powders were ball-milled at 500 RPM in a Retsch PM100 ball mill for a total of 48 hrs. Recurrent pauses of 10 min were used after 10 min of milling to prevent overheating of the samples, along with directional changes to ensure a more homogeneous mixing. The ball milling product was used as the final powder sample.

The powders obtained by ball milling were used for characterisation, as well as for the further preparation of pellets and films. These powders were dissolved in a mixture of DMF and NMP to prepare a solution for spin-coating thin films. As a reference, a solution was also prepared by dissolving the precursor iodides (prior to ball-milling) in stoichiometric ratios to produce spin-cast films. Both sets of solutions were used to prepare thin films with the same synthesis parameters. However, no single phase was obtained from dissolving the iodides directly (without ball-milling), and was therefore not pursued further. A possible reason for this may be changes in oxidation states of certain cations, driven by the energy released during ball milling, which is crucial for the formation of the high-entropy phase.

Pellet synthesis: The as-prepared powders were pressed into pellets using an 8 mm die in a uniaxial press under a pressure of 200 MPa for 5 min.

Film synthesis: The as-prepared ball-milled powder was dissolved in a 1:1 (v/v) mixture of dimethylformamide (DMF) and N-methyl-2-pyrrolidone (NMP) to obtain a 0.3 M precursor solution for spin coating. The quartz substrate used for spin-coating was cleaned with water, acetone, and isopropanol for 15 min, followed by plasma treatment for 5 min. The precursor solution was spin-coated onto the substrate inside an argon glovebox (Jacomex, <10 ppm O_2 and <1 ppm H_2O) at 3000 RPM for 30 s. This substrate was then dried on a hot plate at 110 °C inside the glovebox to obtain an HEI thin film. For reference, solutions of the precursors (prior to ball-milling) were spin cast on plasma-treated quartz substrates at 3000 RPM for 30 s in a glovebox with an argon atmosphere. The substrates were then dried at 110 °C on a hot plate.

4.2. X-ray diffraction (XRD)

Powder XRD for final products of ball milling were collected using a D8 diffractometer (Bruker) with a Cu-$K_{\alpha1,2}$ radiation source. The measurements were performed for the angular range of 10° – 90° with the Bragg-Brentano geometry. The refinement was carried out using Topas Academics V5 software.

Powder XRD diffraction patterns for the aliquots from ball milling were collected using a Stadi P diffractometer (STOE), equipped with a Ga-jet X-ray source (Ga-Kβ radiation, 1.2079 Å). The patterns were measured in the reflection mode, between 10 and 80° with a 0.02° step size. The powders were fixed with Kapton foil to protect against atmospheric degradation.

4.3. Attenuated total reflection infrared (ATR-IR) spectroscopy

ATR-IR spectroscopy was performed on powder samples using a Nicolet iS50 ATR FT-IR spectrometer (Thermo Scientific) in the range 4000 – 400 cm^{-1}.

4.4. Photoelectron spectrometry in air (PESA)

Ionisation potential (IP) measurements were performed using an AC-2E photoelectron spectrometer (Riken Keiki) on pressed pellet samples. The photoelectron yields were corrected for the quantity of light and fitted with a power number of 0.5 to obtain the IPs. The data collected from photoelectron yield (Y) against excitation energy (hv) is fitted using a regression model, $Y = (hv\text{-}IP)^n$.

4.5. UV–vis spectrometry

Absorbance measurements were performed on a UV–Vis-NIR spectrometer (Cary 5000, Agilent) with a double-beam setup. Spin-coated films were used for measurements in the transmission mode.

4.6. Scanning electron microscopy (SEM)

SEM imaging was performed using a Gemini Leo 1530 scanning electron microscope (Carl Zeiss) with an accelerating voltage of 5 kV to minimise sample degradation under the electron beam.

4.7. Atomic force microscopy (AFM)

The AFM images were obtained on a Dimension Icon AFM (Bruker) in tapping mode under inert conditions and processed with the NanoScope 9.7 software.

4.8. X-ray fluorescence (XRF)

XRF measurements were conducted using an XGT-9000 micro-XRF analyser (HORIBA) on powder samples under vacuum.

4.9. Hardness measurements

Hardness and Young's modulus were determined using an iNano Nanoindenter (KLA) equipped with a Berkovich-shaped diamond tip. Before nanoindentation, the instrument was calibrated using a standard fused silica reference sample. Measurements were performed at room temperature in load control mode with a peak load of 10 mN at a strain rate of 0.2 s^{-1} and a dwell time of 10 s at maximum load. For each sample, 20 indentations were conducted. Resulting load-depth curves were analysed using the standard Oliver-Pharr method [45] to determine Young's modulus and hardness values.

CRediT authorship contribution statement

Anurag Khandelwal: Writing – original draft, Investigation, Conceptualization. **Evgeniy Boltynjuk:** Writing – review & editing, Investigation, Conceptualization. **Holger Röhm:** Writing – review & editing, Investigation. **Simon Schweidler:** Writing – review & editing, Supervision, Investigation, Conceptualization. **Alexander Colsmann:** Writing – review & editing, Validation, Supervision, Funding acquisition, Conceptualization. **Jasmin Aghassi-Hagmann:** Writing – review & editing, Supervision, Funding acquisition. **Ben Breitung:** Writing – review & editing, Writing – original draft, Supervision, Funding acquisition, Conceptualization.

Declaration of competing interest

The authors declare that they have no known competing financial interests or personal relationships that could have appeared to influence the work reported in this paper.

Acknowledgments

The authors acknowledge funding by the Carl Zeiss Foundation (project KeraSolar). H.R. and A.C. appreciate the support from the Helmholtz research program “Materials and Technologies for the Energy Transition" (MTET). J.A.-H. acknowledges funding by the DFG under Germany’s Excellence Strategy via the Excellence Cluster “3D Matter Made to Order” (EXC-2082/1–390761711). The KLA nanoindenter iNano was supported by 3DMM2O - Cluster of Excellence (EXC-2082/1 – 390761711). S. S. acknowledges funding from the German Federal Ministry of Research, Technology and Space (BMFTR) in the Nano-MatFutur program within the project MAP-KAT (03XPM025).

Supplementary materials

Supplementary material associated with this article can be found, in the online version, at doi:10.1016/j.mtla.2026.102860.

References

[1] J.W. Yeh, et al., Nanostructured high-entropy alloys with multiple principal elements: novel alloy design concepts and outcomes, Adv. Eng. Mater. 6 (2004) 299–303.
[2] B. Cantor, I.T.H. Chang, P. Knight, A.J.B. Vincent, Microstructural development in equiatomic multicomponent alloys, Mater. Sci. Eng. A 375–377 (2004) 213–218.
[3] C.M. Rost, et al., Entropy-stabilized oxides, Nat. Commun. 6 (2015).
[4] C. Oses, C. Toher, S. Curtarolo, High-entropy ceramics, Nat. Rev. Mater. 5 (2020) 295–309.
[5] S. Schweidler, et al., High-entropy materials for energy and electronic applications, Nat. Rev. Mater. 9 (2024) 266–281.
[6] A.R. Mazza, et al., Charge doping effects on magnetic properties of single-crystal La 1 − x Sr x (Cr 0.2 Mn 0.2 Fe 0.2 Co 0.2 Ni 0.2) O 3 ($0 \leq x \leq 0.5$) high-entropy perovskite oxides, Phys. Rev. B 104 (2021) 94204.
[7] T. Wang, H. Chen, Z. Yang, J. Liang, S. Dai, High-entropy perovskite fluorides: a new platform for oxygen evolution catalysis, J. Am. Chem. Soc. 142 (2020) 4550–4554.
[8] C.R. McCormick, R.E. Schaak, Simultaneous multication exchange pathway to high-entropy metal sulfide nanoparticles, J. Am. Chem. Soc. 143 (2021) 1017–1023.
[9] T. Jin, et al., Mechanochemical-assisted synthesis of high-entropy metal nitride via a soft urea strategy, Adv. Mater. 30 (2018) 1707512.
[10] P. Sarker, et al., High-entropy high-hardness metal carbides discovered by entropy descriptors, Nat. Commun. 9 (2018) 4980.
[11] Q. Wang, et al., Multi-anionic and -cationic compounds: new high entropy materials for advanced Li-ion batteries, Energy Environ. Sci. 12 (2019) 2433–2442.
[12] S. Schumacher, E.V. Alekseev, S. Yu, H. Tempel, R.A. Eichel, High-entropy halides for intercalation battery electrode materials, ChemElectroChem 12 (2025) e202400659.
[13] Z. Song, et al., Promoting high-voltage stability through local lattice distortion of halide solid electrolytes, Nat. Commun. 15 (2024) 1481.
[14] Y. Ye, et al., Advanced high-entropy halide solid electrolytes enabling high-voltage, long-cycling all-solid-state batteries, Nano Lett. 25 (2025) 3747–3755.
[15] F. Temerov, Y. Baghdadi, E. Rattner, S. Eslava, A review on halide perovskite-based photocatalysts: key factors and challenges, ACS Appl. Energy Mater. 5 (2022) 14605–14637.
[16] Y. Hu, et al., Single-mode excited thermally-responsive multicolor emissions of high entropy upconversion perovskite halides for anticounterfeiting, Adv. Opt. Mater. 13 (2025) 2402546.
[17] Y. Cui, et al., High entropy fluorides as conversion cathodes with tailorable electrochemical performance, J. Energy Chem. 72 (2022) 342–351.
[18] S. Li, et al., High-entropy lithium argyrodite solid electrolytes enabling stable all-solid-state batteries, Angew. Chem. Int. Ed. 62 (2023) e202314155.
[19] F. Strauss, J. Lin, A. Kondrakov, T. Brezesinski, High-entropy argyrodite lithium superionic conductors, Matter 6 (2023) 1068–1070.
[20] C.C. Stoumpos, C.D. Malliakas, M.G. Kanatzidis, Semiconducting tin and lead iodide perovskites with organic cations: phase transitions, high mobilities, and near-infrared photoluminescent properties, Inorg. Chem. 52 (2013) 9019–9038.
[21] Y. Tian, et al., High-entropy hybrid perovskites with disordered organic moieties for perovskite solar cells, Nat. Photonics 18 (2024) 960–966.
[22] A.G. Belous, A.A. Ishchenko, O.I. V’yunov, P.V. Torchyniuk, Preparation and properties of films of organic-inorganic perovskites MAPbX3 (MA = CH3NH3; X = Cl, Br, I) for solar cells: a review, Theor. Exp. Chem. 56 (2021) 359–386.
[23] S. Ahmed, et al., Recent trends and challenges in lead-free perovskite solar cells: a critical review, ACS Appl. Energy Mater. 7 (2024) 1382–1397.
[24] Z. Zhang, et al., High-quality $(CH_3 NH_3)_3 Bi_2 I_9$ film-based solar cells: pushing efficiency up to 1.64%, J. Phys. Chem. Lett. 8 (2017) 4300–4307.
[25] C. Motta, et al., Revealing the role of organic cations in hybrid halide perovskite CH3NH3PbI3, Nat. Commun. 6 (2015) 7026.
[26] M. Park, et al., Critical role of methylammonium librational motion in methylammonium lead iodide ($CH_3 NH_3 PbI_3$) perovskite photochemistry, Nano Lett. 17 (2017) 4151–4157.
[27] F.B. Minussi, E.B. Araújo, On the prospects of high-entropy organic A-site halide perovskites, Phys. Chem. Chem. Phys. 26 (2024) 26479–26488.
[28] Y. Song, et al., High-entropy design for 2D halide perovskite, J. Am. Chem. Soc. 146 (2024) 19748–19755.
[29] K. Wang, Y. He, M. Zhang, J. Shi, W. Cai, Promising lead-free double-perovskite photovoltaic materials $Cs_2 MM'Br_6$ (M = Cu, Ag, and Au; M′ = Ga, In, Sb, and Bi) with an ideal band gap and high power conversion efficiency, J. Phys. Chem. C 125 (2021) 21160–21168.
[30] P.A. Sukkurji, et al., Mechanochemical synthesis of novel rutile-type high entropy fluorides for electrocatalysis, J. Mater. Chem. A 9 (2021) 8998–9009.
[31] A.F. Manchón-Gordón, P. Panadero-Medianero, J.S. Blázquez, Descriptors for predicting single- and multi-phase formation in high-entropy oxides: a unified framework approach, Materials 18 (2025) 3862.
[32] Z. Zhu, et al., Interaction of organic cation with water molecule in perovskite $MAPbI_3$: from dynamic orientational disorder to hydrogen bonding, Chem. Mater. 28 (2016) 7385–7393.
[33] T. Leonhard, et al., Probing the microstructure of methylammonium lead iodide perovskite solar cells, Energy Technol. 7 (2019) 1800989.
[34] H. Ma, et al., Supercompliant and soft (CH 3 NH 3) 3 Bi 2 I 9 crystal with ultralow thermal conductivity, Phys. Rev. Lett. 123 (2019) 155901.
[35] Z. Dai, et al., The mechanical behavior of metal-halide perovskites: elasticity, plasticity, fracture, and creep, Scr. Mater. 223 (2023) 115064.
[36] M.Z. Rahaman, A.K.M. Akther Hossain, Effect of metal doping on the visible light absorption, electronic structure and mechanical properties of non-toxic metal halide $CsGeCl_3$, RSC Adv. 8 (2018) 33010–33018.
[37] E. Makagon, R. Merkle, J. Maier, I. Lubomirsky, Influence of hydration and dopant ionic radius on the elastic properties of BaZrO3, Solid State Ion. 344 (2020) 115130.
[38] Y. Liang, et al., Multiple B-site doping suppresses ion migration in halide perovskites, Sci. Adv. 11 (2025) eads7054.
[39] S. Valastro, et al., Temperature-dependent excitonic band gap in lead-free bismuth halide low-dimensional perovskite single crystals, Adv. Opt. Mater. 12 (2024) 2302397.
[40] B. Park, et al., Bismuth based hybrid perovskites $A_3 Bi_2 I_9$ (A: methylammonium or cesium) for solar cell application, Adv. Mater. 27 (2015) 6806–6813.
[41] M. Pazoki, et al., Bismuth iodide perovskite materials for solar cell applications: electronic structure, optical transitions, and directional charge transport, J. Phys. Chem. C 120 (2016) 29039–29046.
[42] S.Y. Kim, et al., Wide range tuning of band gap energy of A3B2X9 perovskite-like halides, Scr. Mater. 166 (2019) 107–111.
[43] M. Ghasemi, et al., Lead-free metal-halide double perovskites: from optoelectronic properties to applications, Nanophotonics 10 (2021) 2181–2219.
[44] P.C. Harikesh, et al., Doping and switchable photovoltaic effect in lead-free perovskites enabled by metal cation transmutation, Adv. Mater. 30 (2018) 1802080.
[45] W.C. Oliver, G.M. Pharr, Measurement of hardness and elastic modulus by instrumented indentation: advances in understanding and refinements to methodology, J. Mater. Res. 19 (2004) 3–20.